Astronomy & Astrophysics

Herschel observations of the debris disc around HIP 92043[*]

J. P. Marshall[1], A. V. Krivov[2], C. del Burgo[3,4], C. Eiroa[1], A. Mora[5], B. Montesinos[6], S. Ertel[7,8], G. Bryden[9], R. Liseau[10], J.-C. Augereau[7], A. Bayo[11], W. Danchi[12], T. Löhne[2], J. Maldonado[1], G. L. Pilbratt[13], K. Stapelfeldt[12], P. Thebault[7,14], G. J. White[15,16], and S. Wolf[8]

[1] Departamento de Física Teórica, Facultad de Ciencias, Universidad Autónoma de Madrid, Cantoblanco, 28049 Madrid, Spain
e-mail: jonathan.marshall@uam.es
[2] Astrophysikalisches Institut und Universitätssternwarte, Friedrich-Schiller-Universität, Schillergäßchen 2-3, 07745 Jena, Germany
[3] Instituto Nacional de Astrofísica, Óptica y Electrónica (INAOE), Aptdo. Postal 51 y 216, 72000 Puebla, Pue., Mexico
[4] UNINOVA-CA3, Campus da Caparica, Quinta da Torre, Monte de Caparica, 2825-149 Caparica, Portugal
[5] ESA-ESAC Gaia SOC, PO Box 78, 28691 Villanueva de la Cañada, Madrid, Spain
[6] Department of Astrophysics, Centre for Astrobiology (CAB, CSIC-INTA), ESAC Campus, PO Box 78, 28691 Villanueva de la Cañada, Madrid, Spain
[7] UJF-Grenoble 1/CNRS-INSU, Institut de Planétologie et d'Astrophysique de Grenoble (IPAG) UMR 5274, 38041 Grenoble, France
[8] Christian-Albrechts-Universität zu Kiel, Institut für Theoretische Physik und Astrophysik, Leibnizstr. 15, 24098 Kiel, Germany
[9] Jet Propulsion Laboratory, California Institute of Technology, Pasadena, CA 91109, USA
[10] Dept. of Earth and Space Sciences, Chalmers University of Technology, Onsala Space Observatory, 439 92 Onsala, Sweden
[11] European Space Observatory, Alonso de Cordova 3107, Vitacura, Casilla 19001, Santiago 19, Chile
[12] NASA Goddard Space Flight Center, Exoplanets and Stellar Astrophysics, Code 667, Greenbelt, MD 20771, USA
[13] ESA Research and Scientific Support Department, ESTEC/SRE-SA, Keplerlaan 1, 2201 AZ Noordwijk, The Netherlands
[14] LESIA, Observatoire de Paris, 92195 Meudon, France
[15] Department of Physical sciences, The Open University, Walton Hall, Milton Keynes MK7 6AA, UK
[16] Rutherford Appleton Laboratory, Chilton OX11 0QX, UK

ABSTRACT

Context. Typical debris discs are composed of particles ranging from several micron sized dust grains to km sized asteroidal bodies, and their infrared emission peaks at wavelengths 60–100 μm. Recent *Herschel* DUNES observations have identified several debris discs around nearby Sun-like stars (F, G and K spectral type) with significant excess emission only at 160 μm.
Aims. We observed HIP 92043 (110 Her, HD 173667) at far-infrared and sub-millimetre wavelengths with *Herschel* PACS and SPIRE. Identification of the presence of excess emission from HIP 92043 and the origin and physical properties of any excess was undertaken through analysis of its spectral energy distribution (SED) and the PACS images.
Methods. The PACS and SPIRE images were produced using the HIPE photProject map maker routine. Fluxes were measured using aperture photometry. A stellar photosphere model was scaled to optical and near infrared photometry and subtracted from the far-infrared and sub-mm fluxes to determine the presence of excess emission. Source radial profiles were fitted using a 2D Gaussian and compared to a PSF model based on *Herschel* observations of α Boo to check for extended emission.
Results. Clear excess emission from HIP 92043 was observed at 70 and 100 μm. Marginal excess was observed at 160 and 250 μm. Analysis of the images reveals that the source is extended at 160 μm. A fit to the source SED is inconsistent with a photosphere and single temperature black body.
Conclusions. The excess emission from HIP 92043 is consistent with the presence of an unresolved circumstellar debris disc at 70 and 100 μm, with low probability of background contamination. The extended 160 μm emission may be interpreted as an additional cold component to the debris disc or as the result of background contamination along the line of sight. The nature of the 160 μm excess cannot be determined absolutely from the available data, but we favour a debris disc interpretation, drawing parallels with previously identified cold disc sources in the DUNES sample.

Key words. Infrared: stars – circumstellar matter – Stars: individual: HIP 92043 (110 Her, HD 173667)

1. Introduction

Debris discs around main sequence stars are the dusty by-products of planetesimal formation processes. This is inferred from the lifetimes of the dust grains that constitute the disc being much shorter than the stellar age (Backman & Paresce 1993). The dust grains are thought to be replenished by collisional attrition of an unseen population of larger bodies, implying the presence of at least asteroid sized objects in these systems (Hahn 2010; Krivov 2010).

The debris discs we typically observe around other stars at far infrared wavelengths are potentially analogous to the Edgeworth-Kuiper belt (EKB) in the solar system. If viewed from afar, the EKB would appear to be a cold ($T \sim$ 40–60 K), very faint ($L_{IR}/L_\star \sim 10^{-7}$) and extended ring of dust (Vitense et al. 2011, 2012) with a central void created by the sculpting action of the giant planets (Moro-Martín & Malhotra 2005). Most of the debris discs that have been observed heretofore have higher dust temperatures and larger fractional luminosities than our own EKB (e.g. q^1 Eri, Liseau et al. 2010; HD 207129,

---

[*] *Herschel* is an ESA space observatory with science instruments provided by European-led Principal Investigator consortia and with important participation from NASA.

Table 1. Physical properties of HIP 92043.

Parameter	Value
Distance	19.2 ± 0.2 pc
Spectral type and luminosity class	F6 V, F5 V – F7 IV
$V, B-V$	4.19, 0.48 mag
Absolute magnitude M_V, bolometric correction	2.77, 0.00 mag
Bolometric luminosity, L_*	$6.14\ L_\odot$
Effective temperature, T_{eff}	6431 K
Surface gravity, $\log g$	4.08
Radius, R_*	$2.0\ R_\odot$
Metallicity, [Fe/H]	0.04
Projected rotational velocity, $\upsilon \sin i$	14.08 km s^{-1}
Rotational period, P	<7.2 days
Activity, $\log R'_{HK}$	–4.90
X-ray luminosity, $\log L_X/L_*$	–5.27
Mass, $M_\star$	1.4–1.7 $M_\odot$
Age	1.6–4.7 Gyr

Fig. 1. Luminosity in $L_\odot$ vs. effective temperature in K over-plotted with isochrones for stellar ages in red (1.4, 1.6, 2.0, 2.5 and 3.2 Gyr, top to bottom) and stellar masses in blue (1.6, 1.4 and 1.2 $M_\odot$, top to bottom). The position of HIP 92043 is marked with a cross.

Marshall et al. 2011; Löhne et al. 2012), a result of the instrumental limitations of current and previous observatories.

We present *Herschel* (Pilbratt et al. 2010) PACS (Photodetector Array Camera and Spectrometer, Poglitsch et al. 2010) and SPIRE (Spectral and Photometric Imaging REceiver, Griffin et al. 2010; Swinyard et al. 2010) observations of HIP 92043 (110 Her, HD 173667), a nearby main sequence Sun-like star. This star is known to have an excess at 70 μm, identified in *Spitzer* MIPS observations (Trilling et al. 2008). We have detected an infrared excess from this target in all three *Herschel* PACS bands, the shape of which is inconsistent with its origin being a single temperature (modified) black body, as is the case for typical debris discs (Wyatt 2008). The origin of the excess is therefore open to interpretation as it cannot be clearly attributed to a debris disc at all wavelengths.

Several intriguing debris disc candidate sources have been identified in DUNES *Herschel* PACS and SPIRE observations of nearby stars (Eiroa et al. 2011). These "cold disc candidates" exhibit only marginal excess emission at wavelengths shortward of 100 μm, a peak in the spectral energy distribution (SED) at 160 μm and no detectable sub-mm excess in SPIRE observations. Such sources are dissimilar to typical debris discs identified by *Herschel* and in previous surveys (e.g. Rhee et al. 2007; Trilling et al. 2008). These discs are also faint, complicating their interpretation and therefore not analogous to the cold debris disc candidates identified serendipitously in H-ATLAS observations, which had bright emission in SPIRE bands (Thompson et al. 2010). The unusual excess observed around HIP 92043 may therefore be the result of a star with two debris belts, one belt with typical properties responsible for the excess at 70 and 100 μm, and a second belt being the dominant contributor to emission at 160 μm. Alternatively, the excess associated with HIP 92043 may be the result of chance alignment with a background galaxy or other contaminant.

In Sect. 2, we present the data reduction and analysis starting with the *Herschel* PACS and SPIRE observations following with the stellar physical parameters and photosphere model and finally a summary of the flux, noise and source extent measurements. In Sect. 3, the results of the analysis are presented from which we derive simple disc parameters and the spatial extent of the source at PACS wavelengths. In Sect. 4, we discuss the possible origins of the emission and, assuming a circumstellar origin for the emission, argue that the properties of the underlying dust grains and their size distribution which might account for the shape of the observed SED are non-standard. In Sect. 5
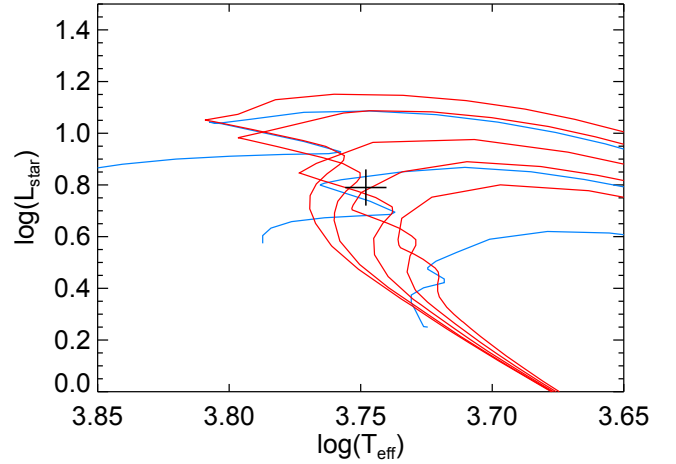
we summarise our findings and present future directions for further study of similar objects.

2. Observations and analysis

2.1. Stellar parameters

HIP 92043 is a main sequence star located at a distance of 19.2 ± 0.2 pc from the Sun (van Leeuwen 2007), classified as spectral type F6 V in the Hipparcos catalogue (Perryman et al. 1997) and F5 V by Gray et al. (2001). Table 1 provides the fundamental stellar parameters as well as some other relevant observational properties and characteristics.

The bolometric luminosity has been estimated from the absolute V magnitude and the bolometric correction from Flower (1996); similar values are obtained using the bolometric correction procedure by Masana et al. (2006). Effective temperature, gravity and metallicity are mean values of spectroscopic estimates (Valenti & Fischer 2005; Takeda et al. 2005; Soubiran et al. 2010) obtained using the DUNES VO tool[1] and lie in agreement with Wu et al. (2011). The projected rotational velocity of the star is $\upsilon \sin i = 14.08$ km s^{-1} (Martínez-Arnáiz et al. 2010), corresponding to a rotational period of <7.2 days. It is classified as a non-active star with an activity index of $\log R'_{HK} = -4.9$ (Maldonado et al. 2010). The observed ROSAT X-Ray luminosity, $L_X/L_{bol} = -5.27$, is close to the expected value for such a star (Pizzolato et al. 2003).

The stellar mass can be estimated from its radius and gravity as well as using stellar models, e.g. Padova post main sequence isochrones (Girardi et al. 2002); estimated values are in the range 1.4 and 1.7 $M_\odot$, see Fig. 1 and Table 1. The age of the star can be estimated from the Ca II H & K activity index of Ca II or from theoretical isochrones. The age using the Ca II H & K activity index is 4.7 Gyr (Maldonado et al. 2010), while using Padova isochrones the estimated age lies between 1.6 and 2.5 Gyr, see Fig. 1. The stellar contribution to the total SED was estimated by using a PHOENIX/*Gaia* synthetic stellar atmosphere model (Brott & Hauschildt 2005). After a comparison of the photosphere scaling to various combinations of optical, near infrared, WISE (Perryman et al. 1997; Aumann & Probst 1991; Wright et al. 2010) photometry and *Spitzer* IRS spectrum,

---

[1] http://sdc.cab.inta-csic.es/dunes/searchform.jsp

Table 2. Predicted stellar photospheric flux of HIP 92043.

Normalization	F_{70} [mJy]	F_{100} [mJy]	F_{160} [mJy]
WISE	47.90 ± 2.20	23.47 ± 1.08	9.17 ± 0.42
nIR+WISE	47.34 ± 2.18	23.20 ± 1.07	9.06 ± 0.42
VI+nIR+WISE	47.60 ± 2.19	23.32 ± 1.07	9.11 ± 0.42
IRS	51.17 ± 2.35	25.07 ± 1.15	9.79 ± 0.45

Table 3. Observation log for HIP 92043.

Wavelength [μm]	PA [°]	Obs. IDs	OD[a]	OT[b] [s]
100/160	70/110	1342192775/76	316	180
250/350/500	–	1342204948	495	185
70/160	45/135	1342216399/400	675	180
70/160	70	1342216397	675	90
100/160	110	1342216398	675	90

Notes. [a] Operational day. [b] On-source time per scan.

the model was scaled to the WISE W1+W3+W4 bands as being the optimum (omitting W2 due to the star being saturated in this band). In the case of HIP 92043 the fit to the *Spitzer* IRS spectrum is systematically higher than the others considered here, underestimating the excess emission at far infrared wavelengths, see Table 2. The *Spitzer* MIPS 24 flux is in better agreement with the photospheric normalisation applied here than with the IRS normalisations.

2.2. Far infrared photometry

HIP 92043 was observed by *Herschel* PACS in scan map mode at 70 μm, 100 μm and 160 μm and SPIRE in small map mode at 250 μm, 350 μm and 500 μm, this is summarised in Table 3. PACS observations were taken using the standard mini scan map parameters for point sources: each map consisted of ten 3′ legs separated by 4″ with an instrument slew speed of 20″/s. A concatenated pair of 100/160 scans were taken at instrument array angles of 70° and 110° and a pair of 70/160 scans were taken at 45° and 135°. A different instrument array orientation was used for the 70/160 combination to check that any extension of the source brightness profile at 160 μm was not an artifact of the scanning direction elongating the source along it. A further single observation of the 70/160 and 100/160 filter combinations was taken at position angles of 70° and 110°, respectively to ascertain if the star had no excess emission at the shorter wavelengths in both cases. A single SPIRE small map observation was also taken to look for a rising flux from the source at submm wavelengths.

All observations were reduced interactively using version 10.0.0 of the *Herschel* Interactive Processing Environment (HIPE, Ott 2010) using PACS calibration version 45 and the standard scripts supplied with HIPE. In total, three observations were taken using the PACS 70/160 combination, and three using the PACS 100/160 combination. The PACS images presented here have been created by mosaicking all of the available scans at 70 μm and 100 μm, but only four of the available 160 μm, to wit those that were observed with the 70°/110° telescope array orientation angle pairs.

The individual PACS scans were processed with a high pass filter to remove $1/f$ noise, using filter widths of 15 frames at 70 μm, 20 frames at 100 μm and 25 frames at 160 μm, equivalent to filter scales of 62″, 82″ and 102″, respectively. To prevent removal of source flux, regions in the images with pixel fluxes brighter than a threshold level defined as twice the standard deviation of all non-zero pixels in the image were masked. Finally, the scans were mosaicked to reduce sky noise and striping effects from the individual scans. Systematic position offsets due to the combined scans being taken at different epochs were accounted for in the mosaicking at all three wavelengths by measuring the 100 μm peak position. Final image scales were 1″/pixel at 70 μm and 100 μm, and 2″/pixel at 160 μm, compared to instrument native pixel sizes of 3.2″ for 70 μm and 100 μm, and 6.4″ at 160 μm. Mosaics were also produced at the native pixel scale

allowing measurement of the sky noise to be made independent of the relationship between pixel size and correlated noise scaling factors.

For the SPIRE observation, a single small map centred on the source was observed with five repetitions. The map was created using the naive mapper, following the standard data reduction script found within HIPE. In the SPIRE images, the source was only visible at 250 μm, resulting in a marginal detection.

Our reasoning for neglecting the extra on-source integration time that combining all six 160 μm scans would provide in favour of a subset of the available data is based around our measurement of the rms background noise level (the method of which is detailed below in this section) for different combinations of the available scans. We combined the scans in four different ways: all six scans, the four scans observed in the same mode, which has three quarters of the on-source time of all six scans, the two longest scans and the four shorter scans, both of which have half the on-source time of all six scans combined. Combining all six images we would expect a reduction of $\sqrt{2}$ in the rms noise level over the two longer or four shorter scans and an improvement of ~1.2 over the four 70°/110° scan combination, if we are in the photon dominated noise regime.

Measuring the rms background we find that the combination of the two longest scans has an rms of 9.0 mJy and the four shorter scans have a value of 6.7 mJy, despite having the same effective on-source time. The mosaic produced from the four scans with the same array angle has a lower rms noise of 7.9 mJy, whilst the rms noise in the mosaic produced from combining all the scans together is 6.8 mJy. The measured rms values for each combination does not scale as expected, with the short and long mosaics having different rms values, whilst all the scans combined have an rms equal to that of the short duration scans, despite having twice the on-source duration. It is therefore considered to be of no advantage for the analysis of this target to use *all* the data in combination. Whilst it would seem obvious to use the combination of scans with the lowest rms noise, the noise in those mosaics using data taken with the 45°/135° combination data is invariant with the effective on-source time, leading us to doubt the veracity of the mosaic reconstruction obtained by mixing the observing modes. Thus, based on the rms noise level results, we decided to use the four 70°/110° scans with the recommended observing mode at 160 μm.

Fluxes were measured on both the native and standard scale PACS mosaics using the HIPE internal aperture photometry routines and checked with MIDAS and IDL based procedures. Aperture radii of 4″ at 70 μm, 5″ at 100 μm and 15″ at 160 μm were used. At 70 μm and 100 μm, the aperture radii were selected to provide the highest signal-to-noise ratio (S/N) for a point source, whilst at 160 μm the aperture radius was chosen to be larger than optimum for a point source (8″) in order to contain all the extended emission. The background level and rms
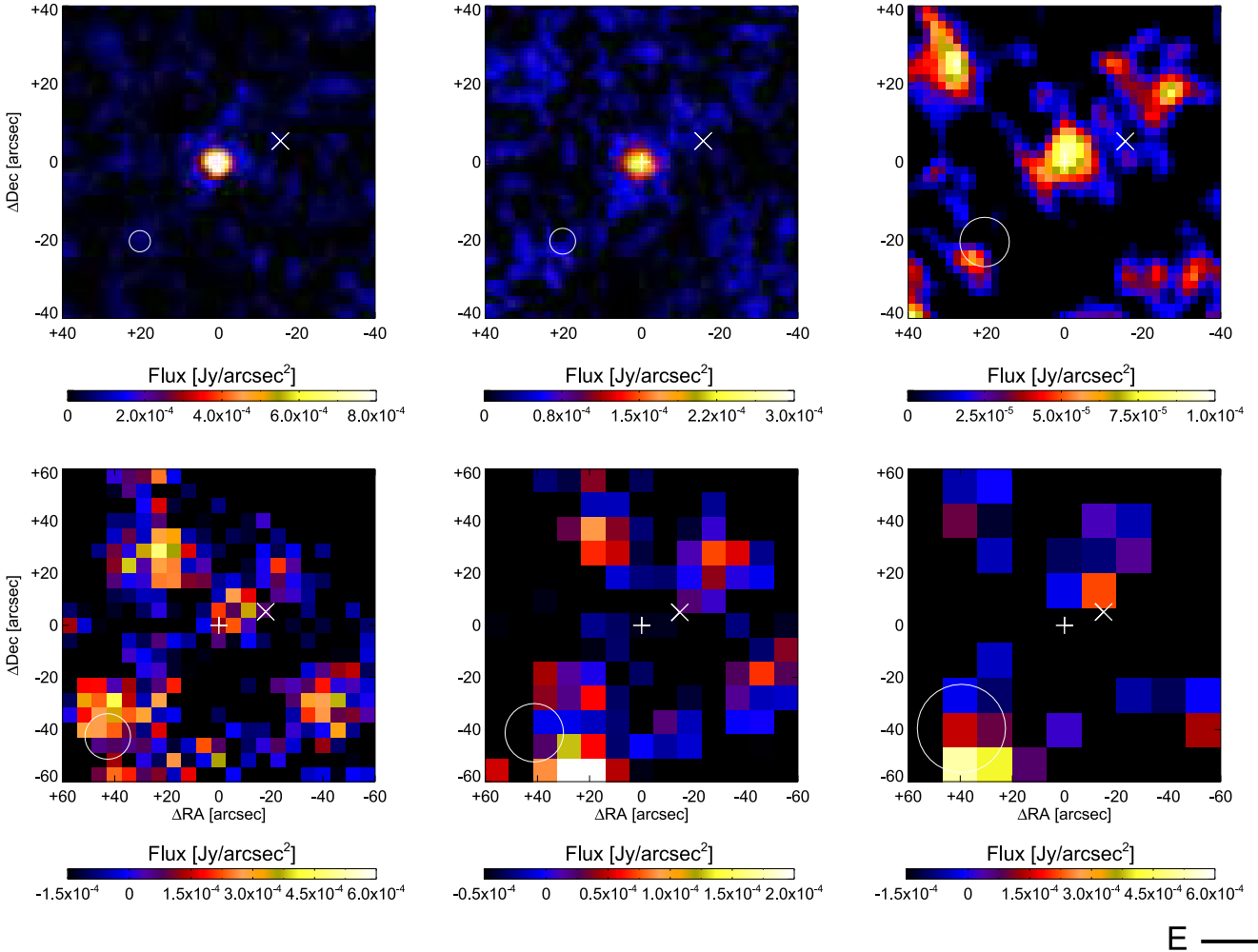
Fig. 2. *Top*: PACS 70, 100 and 160 μm images (*l–r*) of HIP 92043 each covering a region 80″ × 80″ centred on the target. The stellar position is marked with a white "+". A known background source, NVSS J184538+203248, is plotted as a white "×". Instrument beam FWHM is plotted in the bottom left hand corner. Pixel scales are 1″ for the 70 μm and 100 μm images and 2″ for the 160 μm image. *Bottom*: SPIRE 250, 350 and 500 μm images (*l–r*) of HIP 92043 each covering a region 2′×2′ centred on the target. The stellar position is marked with a white cross. Instrument beam FWHM is in the bottom left hand corner. Pixel scales are 6″ for the 250 μm image, 10″ for the 350 μm image and 14″ for the 500 μm image.

sky noise were calculated from the mean and standard deviation of 25 boxes randomly placed around the source position between 30″ to 60″ from the position of HIP 92043. The boxes were sized to match the aperture radius, being 7 × 7, 9 × 9 and 13 × 13 pixels for 70, 100 and 160 μm, respectively. The calibration uncertainty was assumed to be 5% in all three PACS bands. The uncertainties and fluxes were found to be very consistent between the two pixel scales at each wavelength. Appropriate correction factors for the aperture radius (0.476, 0.513 and 0.723 at 70, 100 and 160 μm) and source colour (1.016, 0.989 and – at 70 μm and 1.033, 1.007 and 0.982 at 100 μm; 1.074, 1.042 and 0.976 at 160 μm for the star, warm and cold component contributions) were applied to the measured flux based on the PACS calibration release notes[2].

Fluxes were measured in the SPIRE maps using an aperture with radii of 22″ at 250 μm, 30″ at 350 μm and 42″ at 500 μm and an annulus of 60″ to 90″ for all three bands, centred on the PACS 100 μm peak position. The measured flux was corrected for aperture size and colour as per the SPIRE photometry release

note[3]. A summary of the source photometry is given in Table 4 and the SED and PACS images are presented in Figs. 6 and 2.

At 870 μm we have a constraint on the level of cold excess from HIP 92043 in the form of a 2-σ marginal detection from APEX/LABOCA of 3.6 ± 1.7 mJy/beam (Liseau & Hajigholi, private communication). The LABOCA observation was taken in the point source photometry mode, integrating for 381 min (Programme 087.F-9304(A), PI R. Liseau). This point, along with the SPIRE 250 μm marginal detection and 350/500 μm non-detections rule out the existence of a strong sub-mm excess from this star analogous to the cold debris discs observed by Thompson et al. (2010).

3. Results

The *Herschel* PACS and SPIRE images of HIP 92043 are presented in Fig. 2 and the source photometry is summarised in Table 4. A systematic offset between the two epochs of *Herschel* PACS observations is noted from the differing source positions at 70 μm and 100 μm, the effect of which can be seen in Fig. 4.

Table 4. Summary of the photosphere estimates and infrared archival data, *Herschel* and APEX/LABOCA photometry.

Wavelength [μm]	F_{pred} [mJy]	F_{obs} [mJy]	Instrument	Reference
9	...	3339.0 ± 208.2	AKARI/IRC	1
11	...	2112.0 ± 25.1	WISE/W3	2
12	...	1720.0 ± 172.0	IRAS	3
18	...	770.0 ± 43.6	AKARI/IRC	1
22	...	495.0 ± 6.3	WISE/W4	2
24	...	440.8 ± 15.9	*Spitzer*/MIPS	4
25	...	429.1 ± 5.4	IRAS	3
70	...	69.3 ± 8.9	*Spitzer*/MIPS	4
70	47.9	60.5 ± 3.3	*Herschel*/PACS	5
100	23.5	30.9 ± 2.0	*Herschel*/PACS	5
160	9.2	21.0 ± 8.0	*Herschel*/PACS	5
250	3.8	11.1 ± 7.2	*Herschel*/SPIRE	5
350	2.0	10.2 ± 8.6	*Herschel*/SPIRE	5
500	1.0	3.0 ± 7.6	*Herschel*/SPIRE	5
870	0.3	3.6 ± 1.7	APEX/LABOCA	5

Notes. Uncertainties are 1-σ, including calibration uncertainty and sky rms.

References. (1) Ishihara et al. (2010); (2) Wright et al. (2010); (3) Moshir & et al. (1990); (4) Eiroa et al. (2013); (5) This work.
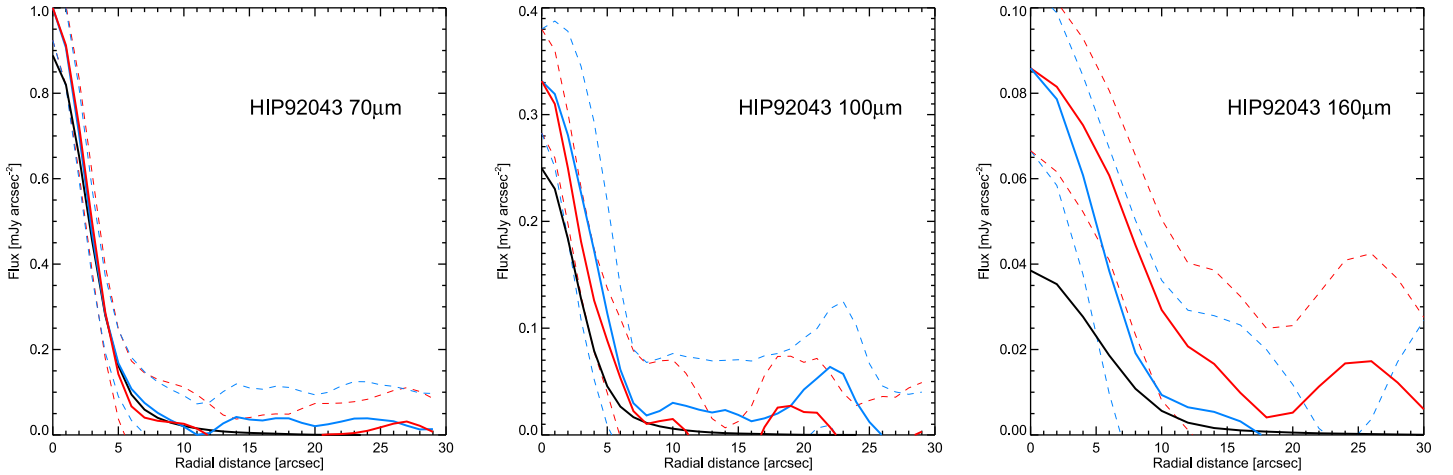

Fig. 3. Radial profiles of HIP 92043 at 70, 100 and 160 μm (l–r), centred on the source peak at each wavelength. The solid red and blue lines represent the average radial profile of the target major and minor axes with their uncertainties denoted by the dashed red and blue lines. The solid black line represents the profile of the PSF model through the same orientation as the target major axis scaled to the predicted photosphere.

At 70 μm, the source brightness profile is point-like. There is a small, 2.1″, offset between the source peak in this mosaic and both the optical and 100 μm position, comparable to the 1-σ *Herschel* pointing accuracy of 2.4″. At 70 μm, *Spitzer* observations of HIP 92043 detected a marginal excess above the photosphere (Bryden et al. 2006). We measure an excess of 3.8-σ at 70 μm, though at a lower total flux level (60 mJy rather than 69 mJy) than the previous *Spitzer* MIPS measurement. The *Herschel* measurement is considered to be more accurate than the *Spitzer* measurement by virtue of the smaller beam size of *Herschel* PACS compared to *Spitzer* MIPS reducing the chance for an overestimation of the source flux due to the inclusion of background flux.

At 100 μm we measure a flux of 30.9 ± 2.0 mJy, equivalent to a 3.7-σ excess. The peak of the stellar brightness profile is consistent with the proper motion corrected stellar optical position within the 1-σ *Herschel* pointing uncertainties. The excess emission is also unresolved at this wavelength and the total of the observed emission is therefore attributable to the same origin as the unresolved emission at 70 μm.

At 160 μm, we measure a flux of 21.0 ± 8.0 mJy, giving a marginal 1.5-σ excess. We also see that the source profile is extended. The peak of the source brightness profile is not coincident with the stellar position, being offset ~1″ to the North (<1/3 of the PSF FWHM at this wavelength), but does encompass the stellar position. Similar offsets are seen between bands in other stars of the DUNES sample (Eiroa et al. 2013). In combination, the 70 and 100 μm excesses which are attributable to a falling dust SED combined with the greater than expected 160 μm flux (if a continuation of the 70/100 component) suggests the existence of two separate cold dust belts around HIP 92043, if the 160 μm flux is not the product of contamination. The case for excess at this wavelength is dependent on the interpretation of the extended structure around the source, which will be addressed in the Discussion section.

The results of the radial profile measurements, characterizing the extended or point-like emission from HIP 92043 at PACS wavelengths are presented in Fig. 3. We produced radial profiles of the source major and minor axis for each wavelength in the following manner: at each wavelength the image was centred
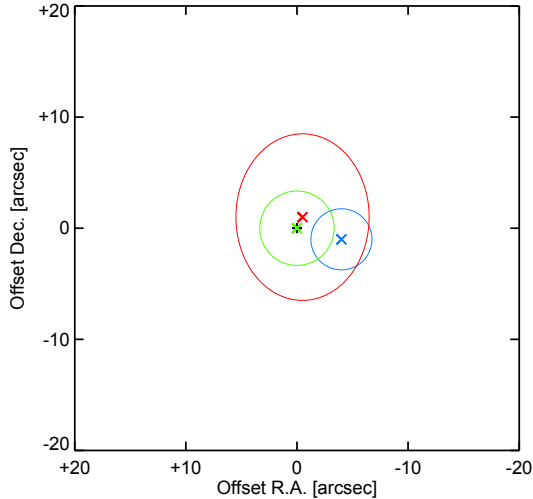
Fig. 4. Source peak positions "×" and half-peak contours (lines) compared to the proper-motion corrected stellar position (black "+") at 70, 100 and 160 μm (blue, green and red).

Fig. 5. *Herschel* PACS 160 μm image of HIP 92043 as observed (*left*) and residual image (*right*) after subtraction of a point source scaled to the predicted source flux from the stellar optical position. Contours in both images are in 1-σ increments of sky noise from −2 to +4-σ (1-σ noise ~3.2 × 10^{-5} Jy/arcsec^2). The light blue contour denotes the flux half-peak contour, as shown in Fig. 4. Image scale is 2″ per pixel and orientation is N up, E left.

on the peak of the source as calculated from the fitting of a 2D Gaussian to the source brightness profile. Each mosaic was then rotated such that the disc major axis (determined from the 160 μm image) lay along the rotated image's *x*-axis. The image was then interpolated to a grid with ten times the density of points, equivalent to spacings of 0.1″ per element at 70 μm and 100 μm and 0.2″ per element at 160 μm. Two regions of this interpolated image on opposite sides of the centre, covering 11 × 11 pixels on a side were summed at distance intervals equivalent to 1″ from the source centre to ±30″ along the image *x*-axis. At each radius increment, the radial profile value was taken as the mean of two diametrically opposed regions and the uncertainty was taken by combining the sky noise (determined from aperture photometry) and difference in the mean of the two regions in quadrature. The same method was applied along the *y*-axis to generate the radial profile of the source along the minor axis. The model PSF images were processed in the same manner to provide a point source radial profile for comparison. We found that both the 70 μm and 100 μm source brightness profiles are consistent with the model PSF. The large uncertainty in the radial profile at 160 μm is a combination of the low S/N of the image and the source not being symmetric through the ellipse centre at this wavelength.

In the mosaicked 160 μm image, the source radial profile is seen to be extended. We fit the extended emission with a 2D Gaussian profile, measuring FWHM for the major and minor axes of 15.0 ± 0.5″ and 12.0 ± 1.4″ along a position angle of 30 ± 15°, using the uncertainty map of the observation to weight the fit to the source brightness profile. We estimate the size of the underlying disc causing the extended profile by subtraction of the source radial profile along the major and minor axis from those of the PSF model.

Adopting a PSF FWHM of 10.57″ by 12.05″ at 160 μm and a distance of 19.2 pc, the spatial extent of the source major axis is estimated as 166 AU, assuming the emission to be circumstellar in origin. Due to the low S/N of the extended emission, the radial profile at 160 μm has large uncertainties. However, it is more extended than a point source along the major axis in which case a minimum size of 108 AU for the source would be inferred at the distance of HIP 92043.
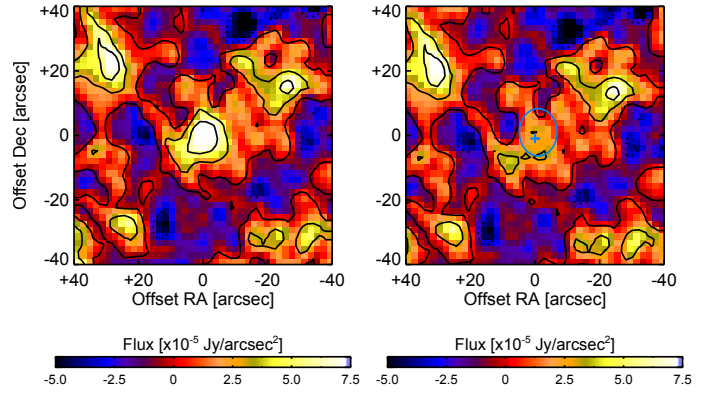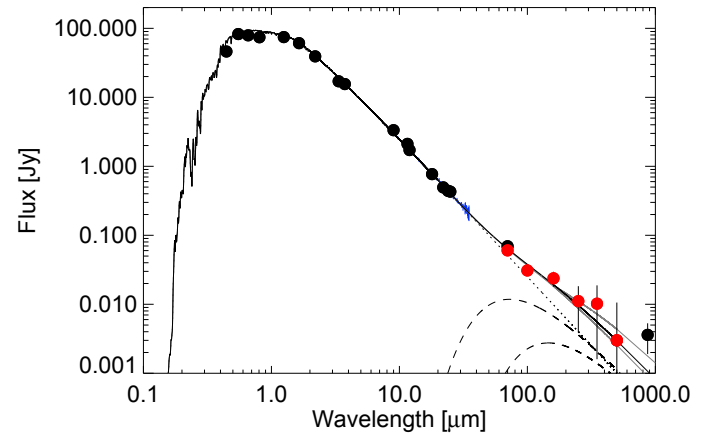
Fig. 6. SED of HIP 92043. Optical, near infrared and LABOCA 870 μm point in black, the *Spitzer* IRS spectrum in blue, *Herschel* fluxes in red. Uncertainties are 1-σ and may be smaller than the data point. The stellar photosphere is denoted by a dotted line. The solid black line denotes the sum of the stellar photosphere and a pair of black bodies (70 and 30 K, dashed lines). The solid grey lines denote the effect on the SED of altering the cold component temperature by ±10 K.

4. Discussion

The observations of HIP 92043 taken by *Herschel* PACS and SPIRE, presented in Sec. 3.1, Fig. 2 and Table 4, suggest the presence of far infrared excess emission at multiple wavelengths. The observed excess, as presented in Sect. 3.2 and Fig. 6, has a shape that is well approximated by a two temperature black body model, consistent with the source being a "cold debris disc" candidate.

However, there are two possible origins for the excess emission, either circumstellar dust around HIP 92043 or background contamination. It is impossible to determine categorically the origin and nature of the excess emission around HIP 92043 with the data currently available. We therefore present here an assessment of the arguments for and against a circumstellar or contamination based origin for the excess exhibited by HIP 92043.
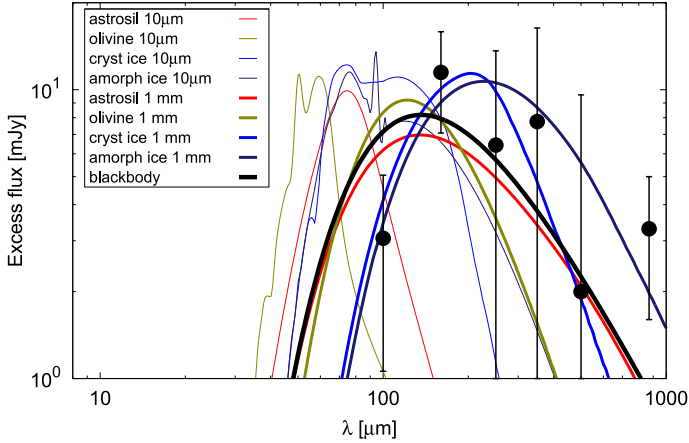
Fig. 7. Excess emission from HIP 92043 plotted with the scaled emission profiles of various standard materials for two grain sizes, 10 μm and 1 mm, at a distance of 130 AU. Fluxes are photosphere and 70 μm dust component subtracted (as described in the text). Error bars on the measurements are 1-σ. It can be seen that the disc should be composed of large, icy (or low optical absorption) and cold grains.

4.1. Background contamination

Contamination by background source(s) is a major stumbling block to the confident attribution of far infrared emission to circumstellar dust and capable of producing the observed excesses and the off-centre source brightness profile seen at 160 μm from HIP 92043.

To check for possible background galaxies, we searched within a region approximately 1′ in radius centered on the stellar optical position for possible X-ray sources in ROSAT data, using NASA's HEASARC system[4]. HIP 92043 has been detected as a strong X-ray source (2RXP J101122.8+492714, 0.16 ct/s). We also searched the same field for optical counterparts using deep optical images from the HST and VLT/NaCo archives and digitized plate scans from the USNO-A and DSS archives, finding no counterparts. NVSS J184538+203248, a background source identified in the NASA Extragalactic Database, is situated 12″ from HIP 92043 but its position is not coincident with any source in the far infrared images and we can therefore ignore it (see Fig. 2).

To quantify the probability of contamination we consider the chance alignment of a source with a flux equal to the measured excess in each PACS band within a circular aperture of equivalent size as the instrument beam. Here we use the source number counts measured for the PACS bands by Berta et al. (2011, their Fig. 7) to estimate the contamination probability per beam. The measured excess fluxes are 12.6, 7.4 and 12.9 mJy and we adopt beam FWHM of 5.6, 6.7 and 11.3″ at 70, 100 and 160 μm, respectively. From these values we calculate incidences of 8.6×10^{-4}, 2.6×10^{-3} and 1.0×10^{-2} sources per beam. Considering the number of targets in the DUNES sample (133) we would not expect to see background sources with the flux level of the excess observed from HIP 92043 at either 70 or 100 μm, with expected contamination incidences of 0.1 and 0.3 sources for a sample the size of the DUNES data set, respectively. At 160 μm, however, the predicted contamination incidence is 1.4 sources and in this instance the presence of a background source cannot be dismissed.

A second, independent estimate of contamination probability can be derived from the statistics of Sibthorpe et al. (2013). In their work the contamination probability at 160 μm of a background source with a flux ~10 mJy within the half-width half-maximum (HWHM) of the source position is estimated as 1.2×10^{-3} (their Table 2), equivalent to 0.16 sources within the DUNES sample. Accounting for the larger source radius (FWHM rather than HWHM), we calculate a contamination probability of 0.8 sources in the DUNES sample, comparable to the estimate derived from Berta et al. (2011) reinforcing the estimate that approximately one source in the DUNES sample suffered such contamination.

4.2. Circumstellar emission

The PACS photometry suggest excess emission from HIP 92043. Furthermore, the shape of the SED suggests that the excess is not well approximated by a single black body. Interpreting the excess as originating from a circumstellar debris disc, we fitted the fluxes with a pair of two parameter ($T, L_{\mathrm{IR}}/L_{\star}$) black bodies. The SPIRE upper limits were treated as inviolable, such that any combination of the black body components that were brighter than the upper limit were rejected outright. Under these assumptions, the excess emission at both 70 μm (11.1 mJy) and 100 μm (8.5 mJy) were reproduced by a single black body with $T_{\mathrm{dust}} = 100$ K. This inner component has a fractional luminosity of 1.6×10^{-6}. At 160 μm, the observed excess emission of 11.8 mJy is larger than the extrapolated contribution from the disc component fitted to the 70 and 100 μm fluxes (4.3 mJy), necessitating the addition of a second, colder disc component to the model. A component with a dust temperature of 25 K satisfies the shortfall in excess emission at 160 μm without violating the (marginal) sub-mm photometry or LABOCA flux point. This second component has a fractional luminosity of 1.8×10^{-7}. The combined two component model with four free parameters (two parameters per component) has $\chi^2_{\mathrm{red}} = 1.4$.

If interpreted as originating from circumstellar dust, the shape of the SED therefore suggests the presence of two dust belts, one peaking in emission around 70 μm and another at 160 μm. The images at 70 μm and 160 μm show different appearance of the emission (point-like vs. extended), it is likely that the 70 μm excess derives from an unresolved inner debris disc. If so, the potential cold disc should be associated mostly with the 160 μm emission. The inner cold belt can be explained as a typical, albeit faint, debris disc approximated here as a black body. For the colder belt, the dust temperature would peak at ~30 K, for which black body dust must be located at distances in the range 70 to 500 AU from the star (assuming a luminosity of $L_{\star} = 6.14\ L_{\odot}$), which is difficult, though not impossible, to explain with plausible dust materials and grain sizes. To get an idea of the properties of the outer, cold component we present the contribution of the cold component to the total excess in Fig. 7, having subtracted the 70 μm-attributable component, overplotted with the expected thermal emission from fiducial discs of equal-sized grains with different optical properties, placed at a distance of 130 AU from an F6 V star. A comparison clearly demonstrates that grains smaller than a few tens of micrometres – those that are expected from collisional models (Krivov et al. 2006; Thébault & Augereau 2007; Müller et al. 2010; Löhne et al. 2012) – yield emission that is too warm to be consistent with the observed fluxes. A rough agreement with the observations can only be achieved for larger grains (≳1 mm), and only if they have low absorption at optical wavelengths (e.g. containing a significant fraction of water ice).

The colder disc component postulated here would be analogous to the "cold debris discs" candidates identified in Eiroa et al. (2011). In addition to the requirement that the grains are large, they should have a low absorption in the visible, perhaps through the presence of icy material on the grain surface. This would cool them to temperatures lower than that of thermal equilibrium at a given radial distance from the star, reproducing the SED's narrow shape. How to maintain a high albedo surface under the action of weathering in a low-collision environment is, however, a problem. Interpretation of the colder component of HIP 92043's debris disc is therefore a significant, but not insurmountable, challenge.

A disc architecture composed of dust grains in a state of low dynamical excitation (small orbital eccentricities and low inclination) was proposed by Thébault & Wu (2008) as a solution to the steep radial profiles of the outer edges of some debris discs. In their model, at very low dynamical excitations ($e < 0.01$), the disc is naturally depleted of small grains due to the disparity between their rate of production (low) and removal (high). This would produce a disc with large grains, effectively "cooling" it.

In a "cold debris disc", where the collisional excitation would be low to limit the dust production rate (accounting partly for the low fractional luminosities), the grains may accrue ice mantles such as those grains in the cold, dense regions of the interstellar medium, or have a high porosity, implying that the "cold debris disc" candidates identified in the DUNES sample would have a far-infrared emissivity per grain higher than that of the standard (Mie) grains studied (or otherwise assumed) heretofore. This would additionally require a lower mass of dust to be present in the disc in order to explain the observed level of far-infrared emission.

The unusual SED of the disc's outer component could also be explained by a circumstellar component wherein the dust grains around this star are atypical in their physical or optical properties (compared to those that match the standard modelling assumptions). This would explain why we have found a candidate "cold debris disc" around one of the more luminous stars in the DUNES sample. For example, the cold grains in debris discs may have enhanced far-infrared emissivities similar to the dust grains in the dense, cold regions of the interstellar medium (see e.g. del Burgo et al. 2003, and references therein).

4.3. Comparison with literature

In this work we measure a flux at 160 μm of 21.0 ± 8.0 mJy, whereas Krivov et al. (2013) quote a flux of 21.9 ± 3.8 mJy, based on the survey measurement from Eiroa et al. (2013). The 160 μm flux measurement presented here, around which much of the analysis is constructed, is therefore seemingly in glaring contrast to the results for HIP 92043 as presented in previous works. Whilst these results are consistent, within uncertainties, the inference may be drawn that the 160 μm flux is of lower significance than previously stated, throwing doubt on the interpretation of this source as a "cold debris disc" candidate. This interpretation would be incorrect for two reasons. As explained in Sect. 2.2, the data combined in this analysis are more than the PACS 100/160 scan and cross scan as used for the DUNES survey at large. Combining additional observations with shorter observing times unsurprisingly increases the measured noise in the final composite image. The method of noise measurement also differs from the survey paper, wherein we have made no effort to exclude regions of faint extended emission present in the field from the noise measurement apertures as was done for the survey paper. The quoted rms sky noise of 7.8 mJy was the mean of 100 separate measurements of the noise, each using 25 randomly scattered apertures across the central 1′ of the field, with a range of 5.5–11.8 mJy. We argue that the true sky noise is at the lower end of this range and that the elevated sky noise measured here is the product of the presence of complex, low-level extended emission in the field due to the proximate location of the source to the galactic plane, rather than an accurate assessment of the intrinsic noise of the sky. Our reasoning for this assessment is that the noise levels at 70 and 100 μm, which do not suffer from the presence of the extended emission visible at 160 μm, have excellent agreement between this work and the survey analysis, despite the different measurement method and data reduction process.

5. Conclusions

We have presented *Herschel* PACS and SPIRE observations of HIP 92043, detecting the presence of significant far infrared excess emission and point-like structure at 70 μm and 100 μm, and marginal excess combined with extended emission at 160 μm, but little emission at wavelengths at 250 μm and beyond, constrained by SPIRE upper limits.

An estimation of the chance of contamination of HIP 92043 by a background source based on the number counts of Berta et al. (2011) demonstrates that a contaminating source with the same flux as the observed 160 μm excess might be expected for at least one source in the DUNES sample. We cannot therefore rule out absolutely a non-circumstellar origin for the 160 μm excess, but note that the expect number of expected contamination events is fewer than the number of cold disc candidates thus far identified (six), from which we infer that the phenomenon is likely real.

We favour the interpretation of this emission as the resulting from the presence of two circumstellar dust belts: an inner debris disc composed of "normal" dust grains and a very faint, outer disc composed solely of larger grains. Using the disc extent provided by the extended emission in the 160 μm images, we constrain the required dust grain properties of the outer belt, finding that large grains with low absorptivity at optical wavelengths provide an acceptable fit to the data.

Standard dust thermal emission models, employing a range of dust grain sizes from microns to millimetres fail to replicate the narrow SED of the outer disc and low dust temperature satisfactorily. A disc composed of large (>100 μm) and high optical albedo grains (such as water ice) can provide a good (though still imperfect) match to the observed SED, but this is by no means the only solution. We have identified several other debris disc sources in our own data which are possibly the result of nonstandard dust grain properties (either material or porosity) and also note that the circumstellar disc of HD 181327, a 12 Myr old F5.5 V β Pic moving group member, is best matched by being composed of large amounts of water ice (Lebreton et al. 2012), suggesting it may be a young progenitor of the disc around HIP 92043. Obtaining evidence of the presence of such materials, through e.g. spectroscopy, is too ambitious for current and near future instruments due to the faintness of the disc.

Future observations by the full ALMA array will be able to resolve the disc extent in both major and minor axes and detect the disc's thermal emission beyond 250 μm, constraining the sub-mm slope of the disc SED and constraining the dust spatial location around HIP 92043. Furthermore, ALMA has the sensitivity to detect the stellar photosphere and could trace the shift in stellar position against any background structure or sources. This would only be feasible after several years due to the low

proper motion of this star. Finally, we direct the reader to the detailed modelling and discussion of the nature of HIP 92043 and other recently identified "cold debris disc" candidates presented in Krivov et al. (2013).

References

Aumann, H. H., & Probst, R. G. 1991, ApJ, 368, 264

Backman, D. E., & Paresce, F. 1993, in Protostars and Planets III, eds. E. H. Levy, & J. I. Lunine, 1253

Berta, S., Magnelli, B., Nordon, R., et al. 2011, A&A, 532, A49

Brott, I., & Hauschildt, P. H. 2005, in The Three-Dimensional Universe with Gaia, eds. C. Turon, K. S. O'Flaherty, & M. A. C. Perryman, ESA SP, 576, 565

Bryden, G., Beichman, C. A., Trilling, D. E., et al. 2006, ApJ, 636, 1098

del Burgo, C., Laureijs, R. J., Ábrahám, P., & Kiss, C. 2003, MNRAS, 346, 403

Eiroa, C., Marshall, J. P., Mora, A., et al. 2011, A&A, 536, L4

Eiroa, C., Marshall, J. P., Mora, A., et al. 2013, A&A, 555, A11

Flower, P. J. 1996, ApJ, 469, 355

Girardi, L., Bertelli, G., Bressan, A., et al. 2002, A&A, 391, 195

Gray, R. O., Napier, M. G., & Winkler, L. I. 2001, AJ, 121, 2148

Griffin, M. J., Abergel, A., Abreu, A., et al. 2010, A&A, 518, L3

Hahn, J. M. 2010, ApJ, 719, 1699

Ishihara, D., Onaka, T., Kataza, H., et al. 2010, A&A, 514, A1

Krivov, A. V. 2010, Res. Astron. Astrophys., 10, 383

Krivov, A. V., Löhne, T., & Sremčević, M. 2006, A&A, 455, 509

Krivov, A. V., Eiroa, C., Löhne, T., et al. 2013, ApJ, 772, 32

Lebreton, J., Augereau, J.-C., Thi, W.-F., et al. 2012, A&A, 539, A17

Liseau, R., Eiroa, C., Fedele, D., et al. 2010, A&A, 518, L132

Löhne, T., Augereau, J.-C., Ertel, S., et al. 2012, A&A, 537, A110

Maldonado, J., Martínez-Arnáiz, R. M., Eiroa, C., Montes, D., & Montesinos, B. 2010, A&A, 521, A12

Marshall, J. P., Löhne, T., Montesinos, B., et al. 2011, A&A, 529, A117

Martínez-Arnáiz, R., Maldonado, J., Montes, D., Eiroa, C., & Montesinos, B. 2010, A&A, 520, A79

Masana, E., Jordi, C., & Ribas, I. 2006, A&A, 450, 735

Moro-Martín, A., & Malhotra, R. 2005, ApJ, 633, 1150

Moshir, M., et al. 1990, in IRAS Faint Source Catalogue, version 2.0

Müller, S., Löhne, T., & Krivov, A. V. 2010, ApJ, 708, 1728

Ott, S. 2010, in Astronomical Data Analysis Software and Systems XIX, eds. Y. Mizumoto, K.-I. Morita, & M. Ohishi, ASP Conf. Ser., 434, 139

Perryman, M. A. C., Lindegren, L., Kovalevsky, J., et al. 1997, A&A, 323, L49

Pilbratt, G. L., Riedinger, J. R., Passvogel, T., et al. 2010, A&A, 518, L1

Pizzolato, N., Maggio, A., Micela, G., Sciortino, S., & Ventura, P. 2003, A&A, 397, 147

Poglitsch, A., Waelkens, C., Geis, N., et al. 2010, A&A, 518, L2

Rhee, J. H., Song, I., Zuckerman, B., & McElwain, M. 2007, ApJ, 660, 1556

Sibthorpe, B., Ivison, R. J., Massey, R. J., et al. 2013, MNRAS, 428, L6

Soubiran, C., Le Campion, J.-F., Cayrel de Strobel, G., & Caillo, A. 2010, A&A, 515, A111

Swinyard, B. M., Ade, P., Baluteau, J.-P., et al. 2010, A&A, 518, L4

Takeda, Y., Ohkubo, M., Sato, B., Kambe, E., & Sadakane, K. 2005, PASJ, 57, 27

Thébault, P., & Augereau, J.-C. 2007, A&A, 472, 169

Thébault, P., & Wu, Y. 2008, A&A, 481, 713

Thompson, M. A., Smith, D. J. B., Stevens, J. A., et al. 2010, A&A, 518, L134

Trilling, D. E., Bryden, G., Beichman, C. A., et al. 2008, ApJ, 674, 1086

Valenti, J. A., & Fischer, D. A. 2005, ApJS, 159, 141

van Leeuwen, F. 2007, A&A, 474, 653

Vitense, C., Krivov, A. V., Kobayashi, H., & Löhne, T. 2011, in EPSC-DPS Joint Meeting 2011, held 2–7 October in Nantes, France, 489

Vitense, C., Krivov, A. V., Kobayashi, H., & Löhne, T. 2012, A&A, 540, A30

Wright, E. L., Eisenhardt, P. R. M., Mainzer, A. K., et al. 2010, AJ, 140, 1868

Wu, Y., Singh, H. P., Prugniel, P., Gupta, R., & Koleva, M. 2011, A&A, 525, A71

Wyatt, M. C. 2008, ARA&A, 46, 339